APPLICATIONS OF THE TRANSILIENT TURBULENCE PARAMETERIZATION TO ATMOSPHERIC BOUNDARY-LAYER SIMULATIONS

R. B. STULL*

Boundary Layer Research Team, Department of Meteorology, University of Wisconsin, Madison, WI, U.S.A.

and

A. G. M. DRIEDONKS**

Royal Netherlands Meteorological Institute, De Bilt, The Netherlands

(Received in final form 21 April, 1987)

Abstract. An improved first-order closure approximation is developed for the non-local 'transilient turbulence' parameterization. Instead of using Richardson numbers, this improved approach uses non-local approximations to the shear, buoyancy, storage, and dissipation terms of the turbulence kinetic energy equation to parameterize the turbulent mixing potential between every combination of grid points in a 1-D model of the atmosphere. The original $(n^2 - n)$ degrees of freedom associated with the independent transilient matrix coefficients for a model of n grid points is thus reduced to four degrees of freedom associated with the four free parameters.

The resulting parameterization is applied to three consecutive case-study days of boundary-layer data acquired near the Cabauw tower in The Netherlands. The first day is used for sensitivity tests to select the best values of the four free parameters. The remaining two days, used as independent tests, demonstrate that realistic entraining mixed layers and nocturnal boundary layers form in the model without explicitly parameterizing such boundary layers. Simulations are also presented for two idealized cases: 'dry' stratocumulus-induced convection and a neutral boundary layer.

1. Introduction

The transilient theory for non-local turbulence closure (Stull, 1984, hereafter S1; Stull and Hasegawa, 1984, S2; Stull, 1986, S3) was developed as an alternative to local closure schemes such as K-theory (Louis, 1979) and higher-order closure (Zeman, 1981; Wyngaard, 1982; Mellor and Yamada, 1982; André *et al.*, 1978). This non-local approach allows large eddies to transport fluid across finite distances before being mixed with the rest of the environment by the smaller eddies.

Both transilient theory and local closure consist of two parts. One part is the general framework, such as a quasi-diffusive transport assumption for K-theory, or a quasi-advective transport assumption for transilient theory. The second part is the closure parameterization itself, such as the functional form for the eddy diffusivity, K, or the form for the transilient mixing coefficients, c. Just as there are many parameterizations for K (see review by Bhumralkar, 1975), there can be alternative parameterizations for c.

* Work performed while a visiting scientist at the Royal Netherlands Meteorological Institute.

** Also: Institute for Meteorology and Oceanography, University of Utrecht, The Netherlands.

Boundary-Layer Meteorology **40** (1987) 209–239.

In the early work by S1 and S2, the transilient coefficients, c_{ij}, were parameterized as a function of the non-local Richardson number, r_{ij}, between points i and j. The assumption behind this was that more mixing should occur in flows that are more dynamically unstable. Although some of the convective mixed-layer simulations based on this approach verified quite well, there existed the possibility that the magnitude of the Richardson number would approach infinity in near-zero wind shear, leaving the transilient coefficients ill-defined or undefined.

Since the Richardson number has its roots in the turbulence kinetic energy (TKE) equation, it was logical to go back to that equation for a better parameterization. It quickly became apparent that the additive nature of the buoyancy and shear terms in that equation were much better behaved than the ratio of those two terms such as in the Richardson number. The derivation (see Section 2) and tests (Sections 3 and 4) of this new approach against observed cases from the Cabauw tower in the Netherlands provided the initial impetus for the research presented here.

Additional questions were raised during this research concerning how dependent the turbulence parameterization was on surface buoyancy fluxes. Were strong surface buoyancy fluxes necessary to drive the turbulence? Would the parameterization work in a weakly forced, or even neutral boundary layer? Would the parameterization work if buoyancy forcings were applied away from the solid boundary, such as at the top of a stratocumulus cloud deck? To examine these questions, a series is idealized simulations were performed, as discussed in Section 5.

The approach taken throughout this study is to test the new transilient parameterization within a one-dimensional numerical model with evenly-spaced grid points in the vertical. Only the discrete (grid-point) form of the theory will be employed. Finally, as with any parameterization, one must examine the sensitivity of the forecast to values of the model parameters, and to grid and timestep resolution. These issues are discussed in Section 6.

2. Transilient Turbulence Parameterization

2.1. Summary of Non-Local Framework

The theory of transilient turbulence has been described in S1, and will be summarized here only to the extent needed for elaborating further on particular aspects encountered in atmospheric applications. Let S be some specific property of the air that is conserved during vertical movement, such as potential temperature, specific humidity, or momentum. If a column of air is split into n equally-spaced grid boxes, then let $S_j(t)$ represent the average value of S within grid box j at time t. During time interval Δt, turbulent mixing can occur between grid box j and any other grid box i. If c_{ij} represents the fraction of air ending in box i that came from box j, then the framework behind non-local mixing is given simply by matrix multiplication:

$$S_i(t + \Delta t) = \sum_{j=1}^{n} c_{ij}(t, \Delta t) S_j(t) \,. \tag{1}$$

As was shown in S1, the sum of each row of elements in c_{ij} must equal unity to satisfy conservation of air mass, as must each column sum to unity to satisfy conservation of property S. Since no element can be negative without violating the increase in entropy of mixing, each element must be $0 \leq c_{ij} \leq 1$ to satisfy all of the above constraints.

2.2. New closure parameterization for transilient coefficients

A new formulation for the transilient coefficients is suggested, based on considerations of turbulent kinetic energy. It is to remembered, however, that we still want transilient turbulence to be a first-order, non-local closure scheme; that is, the only variables that are accessible for the closure formulation are the grid values of the first-order mean quantities, such as mean wind, potential temperature, moisture, etc. Thus the basic non-local framework described by (1) is still used, but the form of the responsive turbulence closure will be improved.

We denote Y_{ij} as a 'mixing potential' between any two grid boxes i and j (equal grid spacing), for $i \neq j$. Furthermore, Y_{ii} is the potential for internal mixing within the grid box i, which acts like a resistance for mixing fluid out of box i. We, furthermore, invoke the exchange hypothesis, $Y_{ij} = Y_{ji}$, so that (Y) is a symmetric matrix.

We define the transilient coefficients c_{ij} by:

$$c_{ij} = Y_{ij} / \| Y \| \quad \text{for } i \neq j\,, \tag{2a}$$

with

$$c_{ii} = 1 - \sum_{\substack{j=1 \\ j \neq i}}^{n} c_{ij}\,, \tag{2b}$$

where n denotes the number of grid points, and $\| Y \|$ is some suitable scalar norm of the matrix (Y), still to be defined.

For a parameterization of the mixing potential Y_{ij}, we consider the equation for turbulent kinetic energy, E, in simplified form, where we neglect for the moment the transport terms:

$$\frac{\partial E}{\partial t} = -\overline{u'w'}\frac{\partial U}{\partial z} - \overline{v'w'}\frac{\partial V}{\partial z} + \frac{g}{\theta_v}\overline{w'\theta_v'} - \varepsilon\,, \tag{3}$$

where the Cartesian mean velocity components are (U, V), the kinematic momentum fluxes are $(\overline{u'w'}, \overline{v'w'})$, the kinematic buoyancy flux is $(g/\theta_v)\overline{w'\theta_v'}$, the rate of dissipation is ε, and θ_v denotes the virtual potential temperature. The first two terms on the right represent mechanical production of E, the third term represents buoyancy production or consumption, and the last term represents viscous dissipation.

We now suppose that any static or dynamic instability between any two grid points i and j will generate turbulent kinetic energy on that same scale $|j - i|\,\Delta z$, in order to remove the instability. However, a fraction of this generated energy is dissipated through ε.

Denote E_{ij} as the turbulent kinetic energy on the scale $|j - i|\,\Delta z$, denote $\overline{(u'w')}_{ij}$ as

the turbulent flux on the same scale, etc. Then, write a non-local analogy to (3), integrate over time Δt, and normalize by dividing by E_{ij} to give:

$$\frac{\Delta_t E_{ij}}{E_{ij}} = \left[\frac{\overline{(-u'w')_{ij}}}{E_{ij}} \left(\frac{\Delta U}{\Delta z} \right)_{ij} + \frac{\overline{(-v'w')_{ij}}}{E_{ij}} \left(\frac{\Delta V}{\Delta z} \right)_{ij} + \frac{g}{\theta_{vi}} \frac{\overline{(w'\theta_v')_{ij}}}{E_{ij}} - \frac{\varepsilon_{ij}}{E_{ij}} \right] \Delta_t t \,, \tag{4}$$

where the operator Δ_t denotes a difference over time, and Δ denotes a difference over space in the vertical between levels i and j.

One should recognize the limitations of this approach. The form of (3) is used to suggest the form of an appropriate scaling for the transilient coefficients. While (3) is local in space, (4) assumes that turbulence can be linearly decomposed according to the spatial scale. Also, the third-order term representing turbulent transport of turbulence is neglected, because in this first-order closure parameterization there is no prognostic variable representing the amount of turbulence that can be transported.

We now define three scaling parameters: a time-scale of turbulence T_0, a dimensionless parameter R_c relating buoyancy to shear, and a dimensionless dissipation factor D, such that:

$$\frac{\overline{(-u'w')_{ij}}}{E_{ij}} = T_0 \left(\frac{\Delta U}{\Delta z} \right)_{ij} , \tag{5a}$$

$$\frac{\overline{(-v'w')_{ij}}}{E_{ij}} = T_0 \left(\frac{\Delta V}{\Delta z} \right)_{ij} , \tag{5b}$$

$$\frac{\overline{(-w'\theta_v')_{ij}}}{E_{ij}} = \frac{T_0}{R_c} \left(\frac{\Delta \theta_v}{\Delta z} \right)_{ij} , \tag{5c}$$

$$\frac{\varepsilon_{ij}}{E_{ij}} = \frac{D}{T_0} . \tag{5d}$$

This approximation brings the equation to first order, as desired for closure.

Since the left-hand side of (4) is a measure of the change of energy associated with turbulent mixing, the right-hand side of (4) can be interpreted as the mechanisms that drive that change. For example, if in the absence of external forcings, a turbulent flow becomes nonturbulent during period $\Delta_t t$ because shears and dynamic instabilities are reduced by the mixing process itself, then the right-hand side of (4) is a measure of the ability of the instabilities to cause mixing before turbulence ceases. This conceptual picture is extended here to define the right-hand side of (4) as a mixing potential, Y_{ij}. Combining (4) and (5) in light of this hypothesis gives:

$$Y_{ij} = \frac{T_0 \Delta t}{(\Delta z)_{ij}^2} [(\Delta U)_{ij}^2 + (\Delta V)_{ij}^2 - (g/R_c \theta_{vi})(\Delta \theta_v)_{ij}] - D \, \Delta t / T_0 \quad \text{for } i \neq j \,. \tag{6}$$

We realize that when we interpret T_0 as a time-scale of the turbulence, then T_0 might also depend on flow or model characteristics such as $(\Delta z)_{ij}/E_{ij}$. However, we chose a

constant time-scale to force the parameterization to be invariant with flow state. Although we used $T_0 = 1000$ s in the Cabauw case studies of Section 4, we find that the model is relatively insensitive to T_0 for $100 \text{ s} \leq T_0 \leq 1000$ s. Since $T_0 = 100$ s also seemed to give the best results for the neutral case studies of Section 5, we recommend $T_0 = 100$ s as best compromise. Of the other two parameters, R_c is analogous to a critical Richardson number, above which turbulent mixing is zero ($Y_{ij} = 0$). Theoretical and laboratory studies give a range of values for critical Richardson number between 0.2 and 1.0, with most suggested values between 0.21 and 0.25. We use $R_c = 0.21$ based on Thorpe's recent arguments. Finally, D is a dimensionless factor that scales the dissipation. Based on the sensitivity arguments expressed in Section 6, we take $D = 1$.

Having defined Y_{ij} for $i \neq j$ with (6), we still are left with the formulation of Y_{ii}. We can interpret Y_{ii} as the subgrid-scale (internal) mixing potential for eddies smaller than the size of one grid box. Since there is little guidance for parameterizing Y_{ii} because it is at a scale below the resolution of the model, we have to rely on some physical considerations that lead to realistic behavior. First, observations of real and laboratory boundary layers suggest that even in the most convective situations, the turbulent structures cause the mean boundary-layer state to become well mixed, rather than to be convectively overturned. This constraint requires that the values of the Y_{ij} elements increase monotonically from the value of the upper right-most element in the (Y) matrix toward the values on the main diagonal, and that Y_{ii} be larger than any other element in the same row; i.e., $Y_{ii} > Y_{i,i+1}$ (see examples in S1).

To find out just how much larger Y_{ii} should be than $Y_{i,i+1}$, we must further add a reference potential Y_{ref} that accounts for the potential for internal mixing within box i. This reference potential should be independent of timestep and grid size. Based on the sensitivity studies discussed in Section 6, we suggest $Y_{\text{ref}} = 1000$ to be of the correct order of magnitude. For comparison, typical $Y_{i,i+1}$ values range from 3000 for strong convective turbulence through 20 for weak nocturnal turbulence. Thus, the final parameterization for internal mixing potential is

$$Y_{ii} = \max(Y_{i,i-1}, Y_{i,i+1}) + Y_{\text{ref}}. \tag{7}$$

In defining a suitable scalar norm $\| Y \|$, we normalize by the maximum sum $\Sigma_j Y_{ij}$ found in any row in the (Y) matrix. This represents the greatest mixing potential from one grid point to all other grid points.

$$\| Y \| = \max_i \left(\sum_j Y_{ij} \right). \tag{8}$$

As a result, when (6) gives small values for $Y_{ij} (i \neq j)$, the large constant value of Y_{ref} insures that the sum in $\| Y \|$ will be essentially a constant, meaning that there will be little mixing out of any grid box and that the forecast is independent of timestep and grid size. On the other hand, when (6) gives large values of Y_{ij}, then the Y_{ref} value contributes in a small way to the total sum, which allows the norm to float as necessary to insure that mixing but not overturning is the greatest effect of turbulence.

The approach outlined above is a strongly parameterized version of turbulent mixing,

which reduced the numbers of degrees of freedom from $(n^2 - n)$ to 4, where the four parameters are T_0, R_c, D, and Y_{ref}. Further tests on the sensitivity of the results to the choices of T_0, R_c, D, and Y_{ref} are given in Section 6.

We now have defined all the necessary tools to apply this new parameterization to particular problems in the atmosphere. The governing forecast equations for any first-order variable $S(z, t)$ can be solved using traditional methods, except for the portion representing turbulence. Turbulent effects are then included by solving (1), (2), (6), (7), and (8). A typical implementation of transilient mixing is discussed next.

3. Typical Implementation

The purpose of this particular ABL model is to create an environment of atmospheric forcings within which the characteristics of the transilient turbulence parameterization can be observed. A highly simplified model is designed, incorporating only some of the known ABL forcings. The simulation results are thus best interpreted as reactions of the turbulence scheme to the simplified imposed forcings. Other investigators might be able to incorporate the transilient turbulence method into their own more detailed ABL models.

3.1 Model discretization

A one-dimensional model is used with evenly spaced grid points in the vertical. A variety of domain sizes (300 m to 3 km), grid spacings (Δz = 10 to 500 m), and timestep increments (Δt = 5 to 30 min) are used in the following simulations. There are no numerical stability limitations on the relationship between Δz and Δt. All yield an absolutely numerically stable model for the transilient portion of the forecast (S3). Grid-point values of the horizontal velocities, potential temperature, and specific humidity apply to the center of each grid box.

Vertical fluxes apply to the boundaries between grid boxes (i.e., staggered between the other grid points). Although calculation of these fluxes was not required to execute the transilient model, they were computed to provide more insight into the performance of the transilient model. The turbulent kinematic flux, $F_k (= \overline{w' S'})$, across the top of grid box k was diagnosed from

$$F_k = (\Delta z/\Delta t) \sum_{i=1}^{k} \sum_{j=1}^{n} c_{ij}(S_i - S_j) . \tag{9a}$$

This can also be re-expressed as a recursion relation to save computation time, where

$$F_k = F_{k-1} + (\Delta z/\Delta t) \sum_{j=1}^{n} c_{kj}(S_k - S_j) , \quad \text{and} \quad F_0 = 0 . \tag{9b}$$

3.2. Time differencing

The *responsive* concept described in the previous section for closing the transilient model is also carried over to the numerical implementation. To do this, each timestep is split into two parts: one part where external forcings destabilize the flow, and the second part

where turbulence reacts to the instabilities. This is analogous to Le Chatelier's Principle in chemistry.

(1) First, the dynamics, thermodynamics, source effects, and sink effects are applied using an explicit forward time difference. Those that are body forcings are applied at all the appropriate grid points, while those that are boundary conditions are applied to only the top or bottom grid points, as appropriate. For example, all of the surface heat flux during the days goes into warming or cooling the bottom grid point. The relevant equations are summarized in the next subsection.

(2) Second, the transilient turbulence scheme relaxes or partially undoes the instability. Within this step, the wind components and temperature differences are computed between each pair of grid points, from which the terms of the mixing potential function are computed. Then the transilient coefficients are calculated, and used to mix the state variables. The transilient coefficients are recomputed for each timestep based on the state of the flow at that instant. These equations have been listed in the previous section. An example of this split timestep is given by Stull (1987), but using a slightly different parameterization of the Y_{ii} term.

The net result of the split timestep is that continued external forcings are required to achieve continuous turbulence. Otherwise, the turbulence will reduce the static or dynamic instabilities via mixing, causing turbulence to disappear eventually. Superimposed on this reduction of instabilities is the continuous dissipation of turbulence, which also tends to make turbulence decay. A turbulent steady state is possible only if there are continuously applied external forcings.

Since the physics include no advection terms other than those imposed as boundary conditions, and there are no K-theory diffusion terms, the forward time difference is used with no problems of numerical instability.

3.3. Dynamic and Thermodynamic Body Forcings

There are no liquid water physics in the model, and thus no latent heating. For the simulations involving 'dry' stratocumulus clouds, the net radiative flux, R_{net}, is imposed as a body forcing at the grid points that would have corresponded to cloud top, base, or interior as appropriate. There are no 'true' flux calculations.

The resulting simplified equations for horizontal velocity components, potential temperature, and specific humidity of the flow are:

$$U_i(t + \Delta t) = U_i(t) - \left[M_i(t) \frac{\partial U_i(t')}{\partial s} \right] \Delta t + f[V_i(t) - V_{gi}(t')] \Delta t , \tag{10a}$$

$$V_i(t + \Delta t) = V_i(t) - \left[M_i(t) \frac{\partial V_i(t')}{\partial s} \right] \Delta t - f[U_i(t) - U_{gi}(t')] \Delta t , \tag{10b}$$

Time tendency Horizontal advection Coriolis and pressure gradient

$$\theta_i(t + \Delta t) = \theta_i(t) - \left[M_i(t) \frac{\partial \theta_i(t')}{\partial s} \right] \Delta t + [R^{net}_{i-0.5} - R^{net}_{i+0.5}] (\Delta t / \Delta z) , \tag{10c}$$

Time tendency Horizontal advection Radiative flux divergence

$$q_i(t + \Delta t) = q_i(t)\,, \tag{10d}$$

Time tendency

where $M_i(t) = [U_i(t)^2 + V_i(t)^2]^{1/2}$ is the wind speed, and $\partial(\ )/\partial s$ represents the gradient along the wind direction. For the external forcing terms, the mean value theorem has been employed to give a representative forcing that applies over the timestep. This is indicated by t', where $t' = t + 0.5\Delta t$.

None of these equations includes diffusion because it is explicitly handled with the transilient mixing portion of the timestep.

3.4. Boundary conditions

The horizontal temperature gradient components are applied as externally specified boundary conditions. Unfortunately, values for these gradients are known only at the surface. It would be foolish to assume that these same horizontal gradients are maintained at all heights within the model. Therefore, the magnitudes of the horizontal gradients are multiplied by a factor $(n - i)/(n - 1)$, which linearly reduces the gradient from its value at the surface to zero at the top of the model. The horizontal temperature advection term of (10c) is then $[U_i(t)\,\partial\theta_i(t')/\partial x + V_i(t)\,\partial\theta_i(t')/\partial y]\Delta t$.

Geostrophic winds are also specified as external forcings, based on measured surface pressure gradients in the Netherlands. The changes of the geostrophic winds with height are estimated using the thermal wind equation. Thus, both surface geostrophic wind values and surface values for the vertical gradient of geostrophic wind are specified as boundary conditions. The linear decrease of horizontal temperature gradient with height described above results in a corresponding linear decrease of thermal wind with height. Based on these time varying boundary conditions, the U_g and V_g components of geostrophic winds can be calculated at every timestep for each height.

Horizontal advection terms in the momentum equations are also important, but the horizontal velocity gradients are not accurately known for the case studies used. A crude approximation to the velocity gradient is achieved by assuming that the winds change from the modeled values to geostrophic values over a distance Δs. The approximate horizontal velocity gradients then become $\partial U_i(t')/\partial s \approx (U_i - U_g)/\Delta s$ and $\partial V_i(t')/\partial s \approx (V_i - V_g)/\Delta s$.

Mean vertical motions are neglected. Although this simplification is known to be deficient because the subsidence can be of the same order as the entrainment rate for many ABLs, the actual values of subsidence were not measured for the case studies employed here.

Fluxes at the ground (subscript s) are imposed as boundary conditions on the bottom grid point:

$$U_1(t + \Delta t) = U_1(t) + (\Delta t/\Delta z)\overline{u' w'_s}(t')\,, \tag{11a}$$

$$V_1(t + \Delta t) = V_1(t) + (\Delta t/\Delta z)\overline{v' w'_s}(t')\,, \tag{11b}$$

$$\theta_1(t + \Delta t) = \theta_1(t) + (\Delta t/\Delta z)\overline{\theta' w'_s}(t'), \tag{11c}$$

$$q_1(t + \Delta t) = q_1(t) + (\Delta t/\Delta z)\overline{q' w'_s}(t'). \tag{11d}$$

These equations are applied in addition to the body equations given in the previous subsection.

The imposed surface heat and moisture fluxes are based on the observed fluxes for the corresponding case studies. Surface momentum fluxes are calculated from a bulk transfer relation based on the winds at the lowest grid point. The drag coefficient varies with stability following the parameterization of Louis (1979).

In summary, this is a highly simplified boundary-layer model. The main intent here is to demonstrate how the transilient turbulence portion of the model responds to typical atmospheric forcings.

4. Cabauw Case Studies

4.1. Simulation scenario

Presented here are three simulations of boundary-layer evolution based on measurements taken near the Cabauw tower. This 200 m tower is located 50 km southeast of the North Sea coastline at 51°58′ N and 4°56′ E in The Netherlands (Driedonks *et al.*, 1978; Driedonks, 1981). Although the ground is topographically flat within a radius of more than 30 km, there is a wide variation in land use including small villages, meadows, tree lines, rivers and river dikes. The influence of the shoreline was reduced by selecting three case study days (see Table I) with southeasterly winds. The last simulation was ended after only 14 hours because of approaching showers.

TABLE I

Cabauw case studies

Run	Day (1978)	Start time (GMT)	Duration (hr)	Type of run
9.2F	30–31 May	0600	24	Calibration
9.2L	31 May–1 June	0600	24	Test
9.2 M	1 June	0600	14	Test

The first day is used as a calibration simulation, to determine the best values for the free parameters. The last two days are independent test days, where the parameter values are not changed from those selected in the first case. The values used for all three cases are: $R = 0.21$, $T_0 = 1000$ s, $D = 1$, and $Y_{\text{ref}} = 1000$.

A 3 km domain is used for all runs because the observed top of the turbulent boundary layer did not exceed about 2.5 km. Thirty equally-spaced grid points are used with a grid spacing of $\Delta z = 100$ m. The timestep is $\Delta t = 10$ min, and the advection distance is set

to the distance between the Cabauw tower and the sea (Δs = 50 km), because of the usual formation of strong gradients over this region.

4.1.1. *Boundary Conditions*

Heat and moisture fluxes, geostrophic wind, horizontal temperature gradient, and thermal wind are all prescribed based on surface observations taken near Cabauw tower (see Figure 1). The time axis in these and many of the following figures is labeled in relative Julian time, with day 150.0 corresponding to midnight on 30 May, and fractional components such as 0.25 or 0.5 corresponding to 0600 and 1200 GMT, respectively. The surface fluxes of heat and moisture are determined from measured vertical profiles

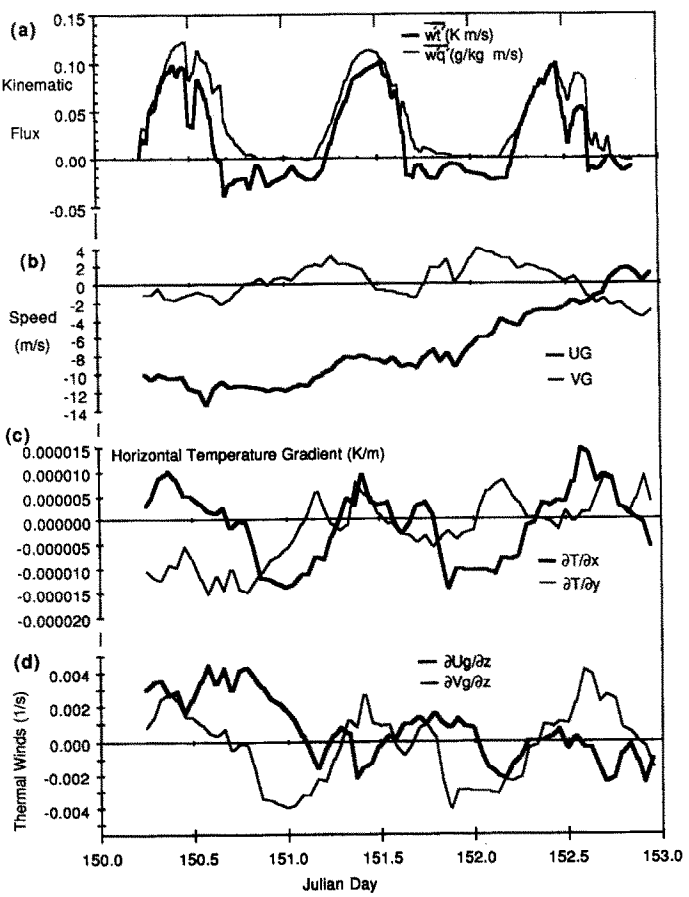

Fig. 1. Observed weather for a three-day period (0600 GMT 30 May to 2200 GMT 1 June, 1978) at the Cabauw tower in the Netherlands, which are applied as boundary conditions to the transilient simulation. The abscissa is time measured in Julian days, where, for example, time 150.5 corresponds to noon on day 150 (30 May). (a) Surface kinematic heat and moisture flux. (b) Surface geostrophic wind components. (c) Surface horizontal temperature gradient components. (d) Calculated vertical gradient of geostrophic wind components near the surface, based on the horizontal temperature gradients of (b).

of mean temperature, humidity, and wind in the surface layer and from energy balance data. The surface geostrophic wind is analyzed by an optimum interpolation method from pressure data at about 20 stations in The Netherlands. The horizontal temperature gradient is analyzed from four weather stations located around the 200 m mast at typical distances of 30 km.

As can be seen from Figure 1, these days all exhibited a strong diurnal cycle of heating during the day and cooling at night. There is a strong geostrophic wind (over 12 m s^{-1}) during the first day, but decreasing to about 3 m s^{-1} during the last day. Thus, the first case is one where both mechanical and thermal generation of turbulence are important, while the last case is one where thermal effects dominate. Figure 1 also shows a strong diurnal cycle in the horizontal temperature gradient, yielding advective heating during the day and cooling at night.

Surface stress is not prescribed, but is calculated using a drag coefficient approach patterned after Louis (1979). An average aerodynamic roughness length of $z_0 = 0.2$ m for the Cabauw tower area is applied for all the wind directions in this study (Nieuwstadt, 1984). The resulting surface drag is based on the thickness of the lowest grid layer (Δz), the stability between that layer and the ground (estimated from the previous timestep), and the wind speed at that lowest grid point.

Horizontal humidity gradients are considered unreliable at all heights, thereby forcing us to set these gradients to zero in the model. Also, subsidence is not known and is set to zero. At night, the direct radiative cooling of the air is also neglected. As a result of these approximations, one should recognize that the dynamics part of the forecast can be in error, thereby causing associated errors in the transilient turbulence response. Nevertheless, the simulations demonstrate the nature of turbulent mixing that can occur in the model in response to changes in the mean state of the boundary layer.

4.1.2. *Initial Conditions*

Cabauw tower measurements and rawinsondes released at 0530–0600 GMT near Cabauw are combined to give detailed composite soundings of θ, q, U, and V at the start of each case-study day. These are then interpolated to the grid point locations (Figure 2) and used to initialize the forecast. The winds at all grid points are initialized to those of the interpolated sounding, and are not set to their corresponding geostrophic values.

4.2. Case Studies

4.2.1. *Run 9.2F: Calibration*

Figure 3 shows the overall behavior of the depth of the boundary layer over a 24-hr period starting at 0600 GMT on 30 May, 1978. Three estimates of boundary-layer depth are plotted based on the transilient model results. One is the maximum contiguous depth of turbulence. During the daytime, this can also be interpreted as the top of the entrainment zone. Two estimates of average mixed-layer height (z_i) are also given during day-time: one based on the height of the most negative heat flux ($\overline{w'\theta'}$), and the other at the height where a rising parcel of surface layer air first becomes neutrally buoyant.

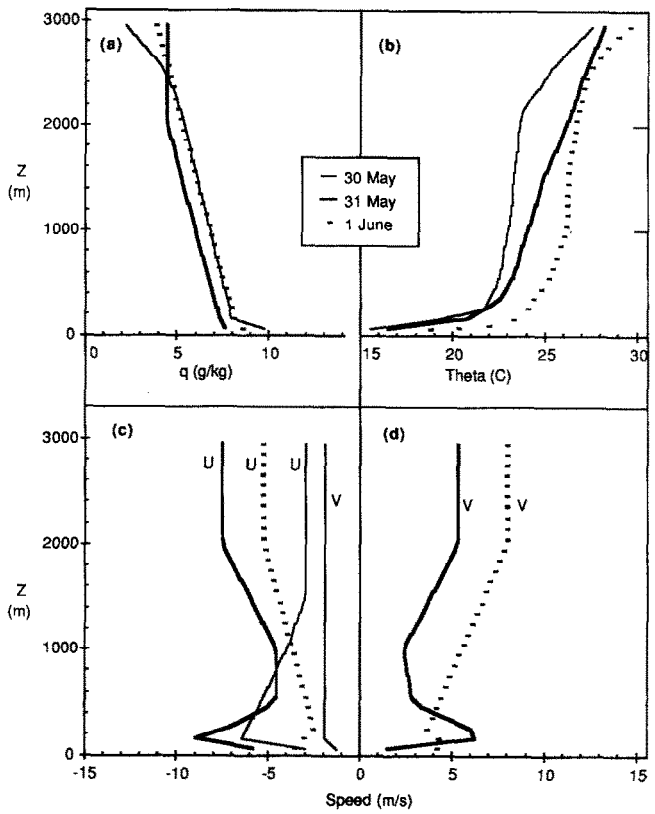

Fig. 2. Observed vertical profiles of mean potential temperature (Theta), specific humidity (q), and wind components (U, V) at 0600 GMT on each on the three case study days. These are used as the initial conditions for the three cases, and also for verification.

For comparson, results are also given from earlier calculations with a bulk mixed-layer model during the day-time (Driedonks, 1982; Driedonks and Tennekes, 1984).

Measured boundary-layer depths from a variety of sensors are also given in Figure 3. Measured depths of turbulence during the night and early morning are taken from a monostatic acoustic echo sounder near the tower. At night, mean temperature data from the tower are used to estimate the top of the statically stable lapse rate of the nocturnal boundary layer. In addition, some radiosondes were released, which unfortunately are scarce in the afternoon period. All of the verification soundings are plotted in Figure 4 for this case. Although the two soundings that were launched from De Bilt (located about 30 km NE of the Cabauw tower) appear consistent with each other, they appear to be representative of a different air mass than the soundings made at Cabauw.

Initially the boundary-layer depth grows only slowly until about 0900 GMT. This initially slow growth is given both by the present transilient model and by the bulk model. The observations virtually coincide with the calculations in this period. After 0900 GMT, however, there is a noticeable difference between the transilient model and

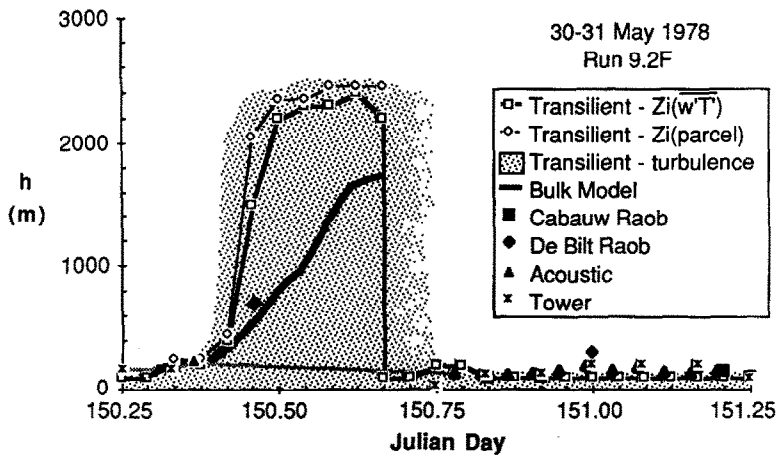

Fig. 3. Comparison of modeled (run 9.2F) and observed boundary-layer depth, h, vs time for one 24-hr period (30–31 May, 1978). The solid lines show two different estimates of modeled daytime average mixed layer depth (z_i, see text): □-points indicate the height where the kinematic heat flux, $\overline{w'T'}$, is most negative; ○-points indicate the height where a parcel rising adiabatically from the surface first becomes neutrally buoyant. The shaded area indicates the extent of modeled turbulence, the top of which is interpreted as the top of the entrainment zone during the day. At night, the top of the turbulence layer (and region where the flux first becomes zero) is used to define h. All available observation data from balloon soundings, the acoustic sounder, and from mean temperature profiles observed at the tower are presented. In addition, z_i from a slab mixed layer model is also plotted for comparison.

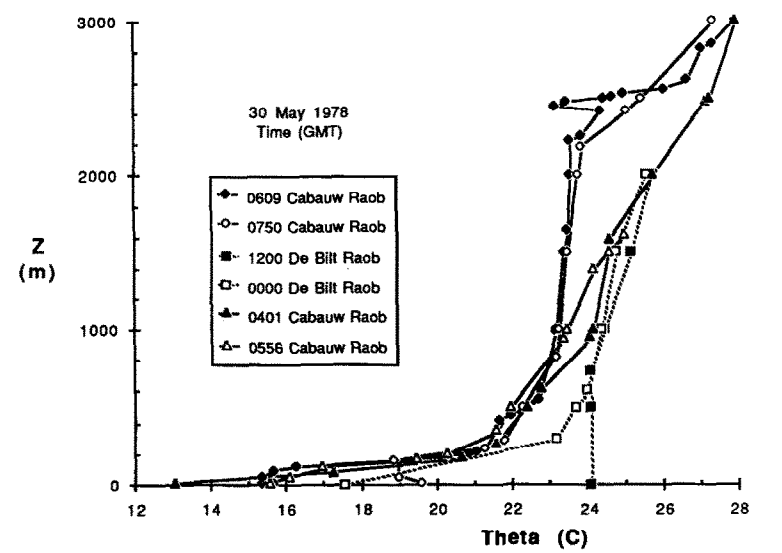

Fig. 4. Observed potential temperature radiosonde soundings taken during 30–31 May, 1978 near the Cabauw tower. Also plotted are soundings from De Bilt (30 km NE of the Cabauw tower).

the bulk model. The transilient results show a very rapid growth of the boundary-layer top to about 2 km between 1000 GMT and noon. This occurs when the top of the mixed layer is rising through the nearly adiabatic regions between 1 and 2 km shown in Figure 4. Then the boundary layer hits an upper air inversion and the depth remains nearly constant during the rest of the afternoon. The bulk model gives a much more gradual increase and significantly lower boundary-layer depths, reaching only about 1 km by noon. The one radiosonde observation of the inversion height is between the transilient and bulk model results.

Figure 5a shows the simulated θ soundings during the day, and also shows the corresponding θ verification measurements made at the Cabauw tower. The afternoon

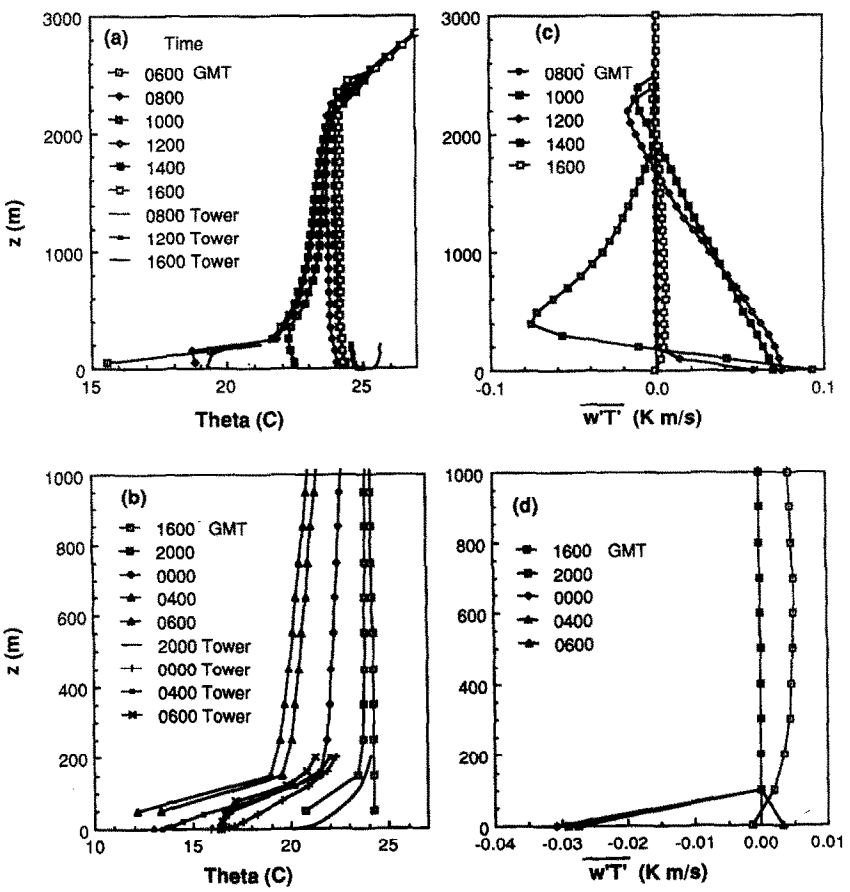

Fig. 5. Modeled (run 9.2F) evolution of vertical profiles of mean potential temperature (Theta) and kinematic heat flux ($\overline{w'T'}$) for 30–31 May, 1978. All times in the legends are GMT. (a) Daytime potential temperature; (b) nighttime potential temperature; (c) daytime heat flux; (d) nighttime heat flux. Also plotted for verification are Cabauw tower observations of theta (up to the top of the tower at 200 m). Note that the height scale for the nighttime diagrams (b) and (d) are expanded to focus on just the bottom third of the modeled domain.

soundings show a typical mixed layer with nearly constant potential temperature, except for some curvature near the top and bottom. Since the simulated mean mixed-layer temperature is about 1 °C cooler than observed and the depth is greater than observed, one would suspect subsidence acting on the real boundary layer. Unfortunately, no information about subsidence was obtained during the Cabauw field program, and thus has not been included in the simulation. In the absence of subsidence for example, a thermal that rises with surface potential temperature of over 25 °C (like that observed) would intercept the morning Cabauw soundings (Figure 4) at about 2500 m, in agreement with the transilient simulation.

Heat flux profiles (Figure 5c) are approximately linear with height within the mixed layer during the free convection conditions of afternoon. The negative flux values near the top of the mixed layer are within the typical free-convective range of -0.1 to -0.3 times the surface value (Stull, 1976; Driedonks, 1982). During the rapid-rise phase of the mixed layer (1000 GMT), we see large negative values of the flux near the mixed-layer top that are associated with the strong shear-generated turbulence and rapid entrainment for this particular case.

During the night, Figure 5b (focusing on only the bottom third of the simulated domain) shows that the imposed horizontal advection of temperature causes a major change in both the stable boundary layer and the overlaying residual layer. The heat flux profiles shown in Figure 5d show that there was no turbulent mixing out of the bottom grid point during most of the night, which agrees with the observed depth of 100–200 m. Although the minimum temperature simulated is less than 1 °C different from the observed surface temperature, the simulated temperature represents an average over a 100 m thick layer, and is thus much colder than the average observed temperature. This might be related to inaccurate specification of temperature advection.

During the evening decay of turbulence in the mixed layer, Figure 5d shows a positive heat flux in the interior of the mixed layer in spite of the negative flux at the surface. A similar response lag of thermals and an associated increase in convective timescale has also been simulated by Nieuwstadt and Brost (1986).

Figure 6 shows the specific humidity and moisture flux profiles during the day. Although there is evaporation from the surface, entrainment of dry air aloft causes a net reduction in mean mixed-layer humidity with time. The slope of the mean humidity profile during the rapid-rise phase of the mixed layer at 1000 GMT and at noon is particularly evident. Even the 1400 and 1600 GMT profiles of humidity show a slight tilt. This is similar to the results from top-down/bottom-up diffusion models (Wyngaard and Brost, 1984). Later in the afternoon when the entrainment moisture flux becomes smaller, the slope of the mean humidity profile also becomes more vertical. The verifying Cabauw tower measurements, also plotted in Figure 6a, indicate a surface layer that is about 2 g kg^{-1} drier than simulated. Again, this might be related to the absence of horizontal moisture advection in the simulation.

Figure 7 gives the U and V components of mean wind. Strong shear evident between 200 and 2000 m in the 0800 GMT profiles becomes mixed into a well-mixed layer in the afternoon profile, with wind shear remaining across the top of the mixed layer. Later

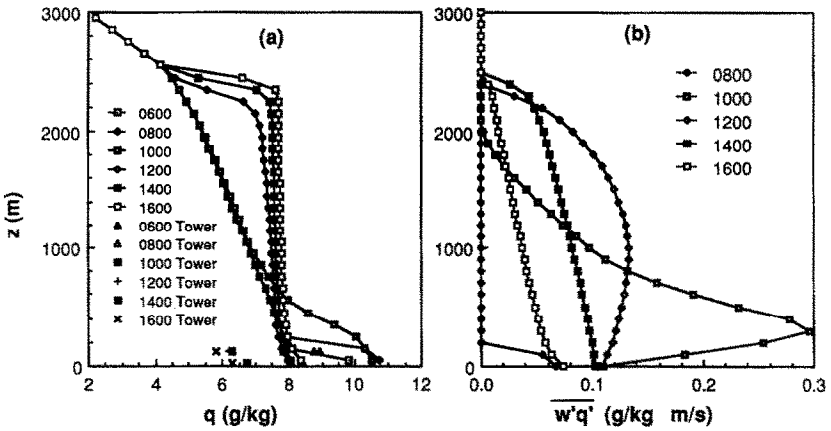

Fig. 6. Same as Figure 5, but for (a) modeled specific humidity, q; (b) modeled kinematic moisture flux, $\overline{w'q'}$, during the daytime hours. Observed humidities at the Cabauw tower are also plotted.

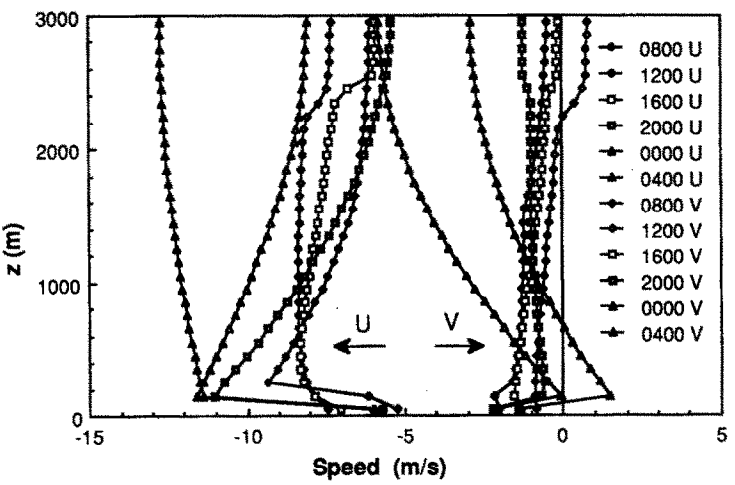

Fig. 7. Same as Figure 5, but for the modeled U and V components of wind.

in the afternoon when turbulence decays over the bulk of the mixed layer, the wind begins its recovery toward geostrophy. A nocturnal jet appears in the simulation at 150 m and is related mostly to thermal wind effects, rather than to inertial oscillations.

Time series of wind speed and direction at selected model grid points are compared with tower measurements in Figure 8. During the daytime, the simulated wind speeds at the lowest grid points are about 1 to 2 m s^{-1} too fast, suggesting that either the drag parameterization is too weak, or the horizontal advection approximation is too strong.

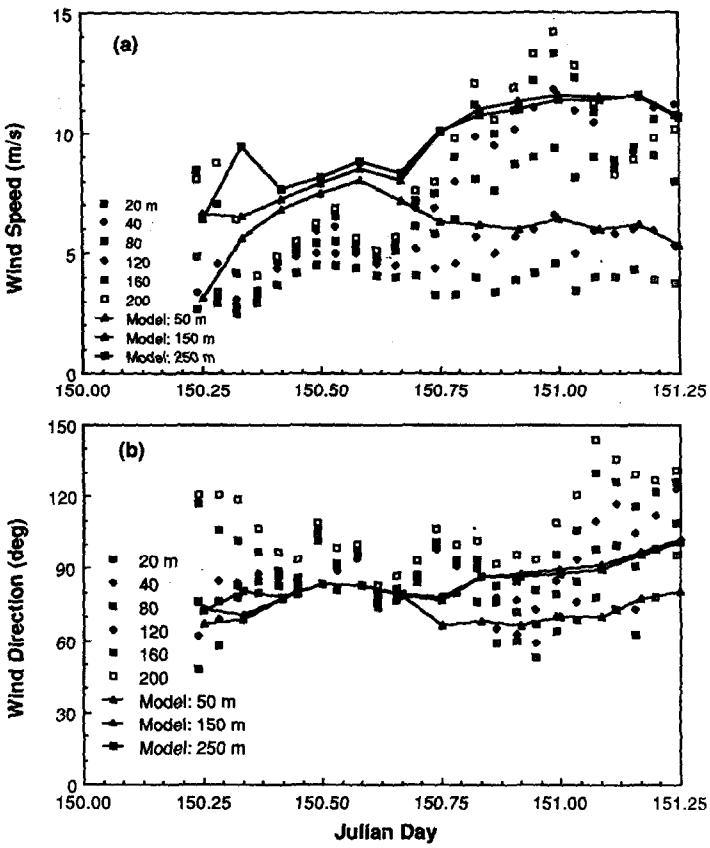

Fig. 8. Comparison of time series of modeled (run 9.2F) and observed (Cabauw tower) wind speed and direction for 30–31 May, 1978.

4.2.2. *Run 9.2L: Independent Test*

Both this simulation and the next were initialized from the observed profiles at the start of the appropriate periods (see Figure 2), not from the simulated profiles calculated at the end of the previous cases.

Figure 9 shows the evolution of boundary-layer depth for the 24-hr period starting at 0600 GMT on 31 May, 1978. Mixed-layer growth is much more gradual during mid-morning than in the previous case, because the advection of temperature created a statically stable lapse rate in the initial residual layer. During the whole period, both the transilient and bulk model are in good agreement with the observations and with each other.

Figure 10 shows the vertical potential temperature profile evolution over the 24-hr simulation, along with verification temperatures from the tower. Simulated boundary-layer temperatures are within about 2 °C of observed temperatures.

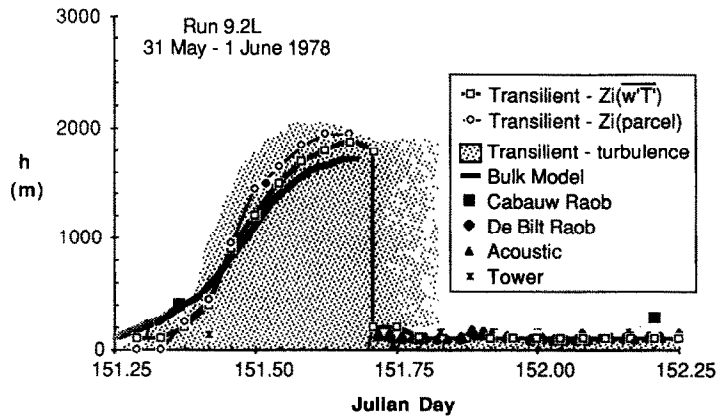

Fig. 9. Comparison of modeled and observed boundary-layer depth for the second case study (run 9.2L, Cabauw, 0600 GMT 31 May to 0600 GMT 1 June, 1978). Similar to Figure 3.

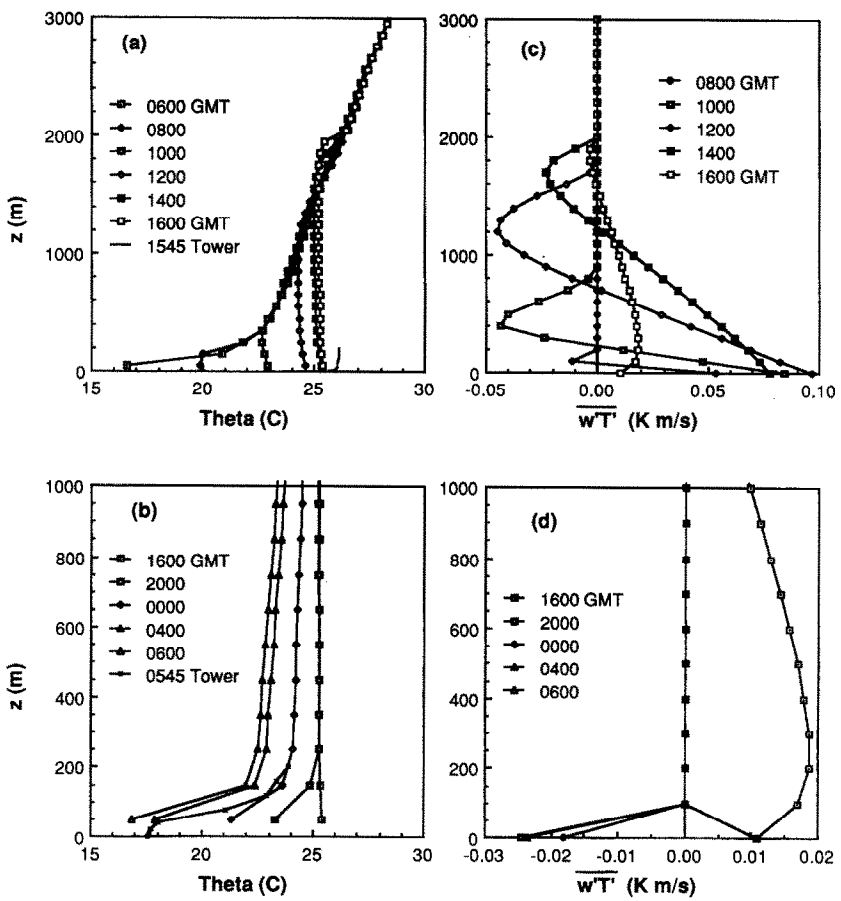

Fig. 10. Modeled vs observed potential temperature and heat flux for the second Cabauw case; 31 May to 1 June, 1978. Similar to Figure 5.

4.2.3. *Run 9.2M: Independent Test*

Figure 11 shows the simulated and observed boundary-layer depth for this case, starting at 0600 GMT on 1 June, 1978. The few observations indicate a slow increase in boundary-layer depth until about 1000 GMT, and then a much faster deepening. Strong shears and weak stability between 1000 to 1500 m cause a clear air turbulence layer to form in the simulation in early morning. Turbulence at those altitudes contribute to the rapid mixed-layer growth at about 1000 GMT.

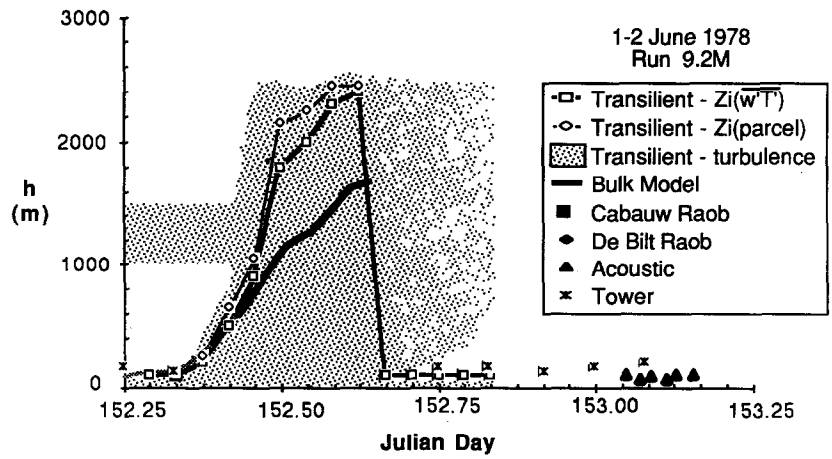

Fig. 11. Comparison of modeled and observed boundary-layer depth for the third case study (run 9.2M, Cabauw, 0600 GMT 2000 GMT 1 June, 1978). Similar to Figure 3.

The transilient and bulk model estimates of z_i agree fairly well during the slow-growth period. The bulk model estimate of z_i grows more gradually after 1000 GMT, while that of the transilient model rises rapidly to a greater height. Decisive verification is again difficult; however, the same arguments apply as in the discussion of the previous two cases related to the role of external forcings in the transilient calculations. The corresponding temperature and heat flux profiles are shown in Figures 12a and 12c.

Figures 12b and 12d show the U-component of wind and momentum flux. The large flux values calculated at 1400 GMT are associated with vertical gradient in geostrophic wind with height (refer to Figure 1). In particular, the geostrophic wind magnitude in the top half of the mixed layer is greater than the mixed-layer value, and the geostrophic wind magnitude in the bottom half is lower. Although the momentum flux curve is positive at all heights (indicating a downward transport of momentum for these easterly winds), the slope of the curve indicates that turbulence is removing easterly momentum from the top half of the mixed layer and is depositing some of it in the lower half of that layer. This is to be expected if the turbulence is to maintain a well-mixed U profile in the presence of a geostrophic wind gradient.

As was mentioned at the start of Section 4, this simulation was terminated early

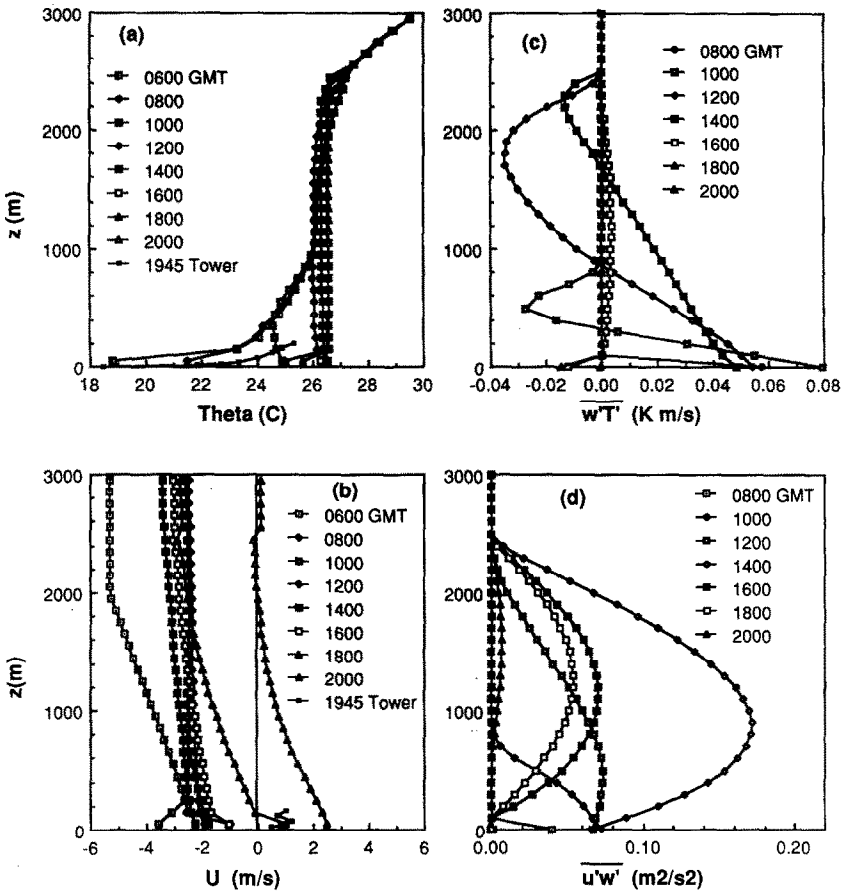

Fig. 12. Modeled vs observed (a) potential temperature and (b) U component of wind for the third Cabauw case; 1 June, 1978. Also plotted are (c) the modeled kinematic heat flux, $\overline{w'T'}$, and (d) the modeled momentum flux component $\overline{u'w'}$.

because of approaching showers. Indeed the 1945 GMT tower measurements show a very cool low-level temperature anomaly that is probably related to cool outflow from the region of showers.

4.3. Discussion

It is clear that the transilient turbulence parameterization is responding to the destabilizing effects of wind shear and surface heating. Although there are no formal equations or parameterizations specifying that there must be a boundary layer, one forms anyway in the model in response to the applied forcings. By not being tied to an explicit assumption regarding shape of the profiles, the transilient scheme is better able to form the non-idealized boundary layers that can occur in windy, advective, disturbed weather conditions. It also appears to handle convection and mixed layers, allowing convective mixing over the whole mixed-layer depth.

As is often the case with real data sets, there are inconsistancies, gaps, and omissions caused by equipment limitations, malfunctions, cost constraints, and technical difficulties. Although the present case studies give a fairly complete picture of the surface layer and the morning boundary layer, they have problems stemming from the measurement and quantification of the external forcings aloft, including subsidence, as well as from a scarity of measurements in the afternoon. As a result, it would be wise to conduct additional verification efforts with other data sets.

5. Idealized Cases

One requirement of a turbulence parameterization is that it must have the ability to react to instabilities generated anywhere within the modeled domain via either buoyancy or shear mechanisms. The previous Cabauw cases were ones where the dominant forcing was buoyant generation near the ground, although there was some shear-induced turbulence aloft. To test the model's capability to react to instabilities generated elsewhere, two idealized situations are presented here: 'dry' stratocumulus convection and a neutral boundary layer.

5.1. 'DRY' STRATOCUMULUS

A 'dry' stratocumulus cloud is modeled with a base at 500 m above the ground, and a top at 1000 m. The present model is not meant to be a complete moist boundary-layer model with radiation and condensation physics. Instead, the *effect* of some of the stratocumulus processes on the generation of turbulence is idealized by applying a prescribed radiation flux divergence that is typical of stratocumulus situations.

Two radiation forcings are presented here. In the first case, a nocturnal stratocumulus is simulated where the prescribed longwave radiation (Figure 13a) causes strong cooling at cloud top, and weak heating at cloud base. The longwave heating and cooling are

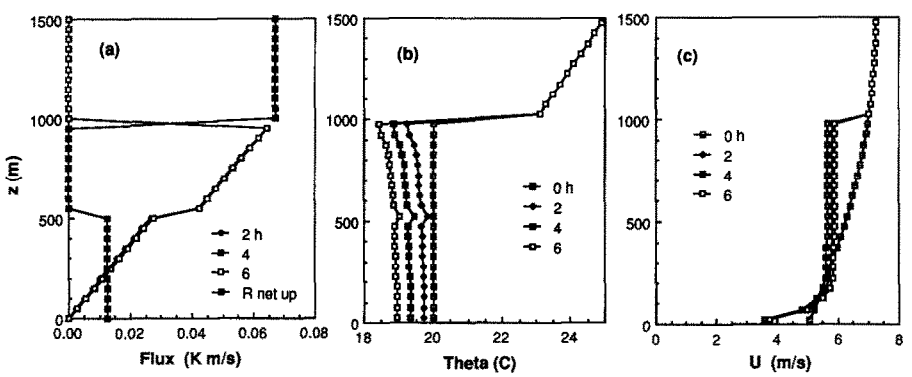

Fig. 13. Simulation of 'dry' nocturnal stratocumulus-topped boundary layer. (a) Modeled kinematic heat flux profiles at 2, 4, and 6 hours into the simulation. Also shown is the imposed radiative flux (R net up) also expressed in kinematic units. Modeled evolution of (b) potential temperature and (c) U wind component profiles.

idealized as occurring in regions only one grid-layer (50 m) thick. At cloud base, there is a net radiative convergence of 15 W m^{-2} causing the warming, while at cloud top there is a net divergence of 80 W m^{-2} causing the cooling.

The second case, a daytime stratocumulus scenario, adds the effect of solar heating within the top of the cloud (Figure 14a), in addition to the longwave radiation described for case one. This addition consists of a radiative convergence of 80 W m^{-2} exponentially spread within the top 400 m of the cloud.

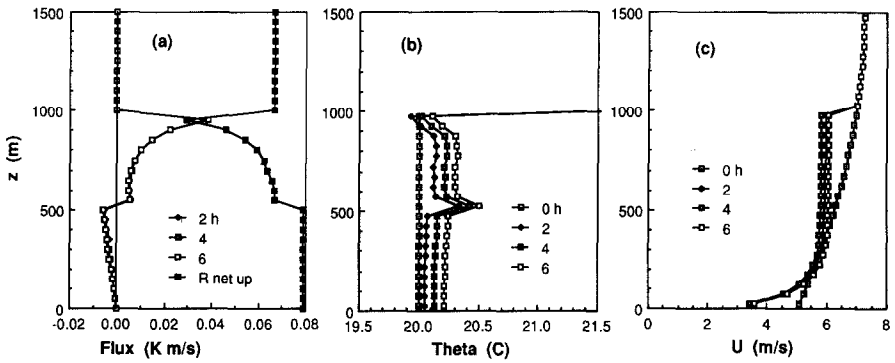

Fig. 14. Simulation of 'dry' daytime stratocumulus-topped boundary layer. Similar to Figure 13.

The initial θ-profiles for both cases (Figures 13b and 14b) consist of an adiabatic lapse rate from the surface to 1 km, with a 3 °C temperature jump at cloud top (i.e., at 1 km). Above that is a statically stable lapse rate of 4 °C km^{-1}. The effect of this strong inversion is to eliminate turbulent entrainment during the 6 hours of forecast, thereby allowing the cloud top location to remain consistent with the applied radiative cooling. For all cases, a surface geostrophic wind of 5 m s^{-1} is used, with a surface thermal wind of 0.003 s^{-1} decreasing to zero at the top of the domain. Thus, at the top of the domain, the geostrophic wind is 7.25 m s^{-1}. The initial wind is set equal to the geostrophic wind for these cases (Figures 13c and 14c). There is no horizontal advection of momentum or heat.

In the following simulations, a grid spacing of Δz = 50 m is used within a vertical domain of 1500 m. A timestep of Δt = 15 min is used to make a 6 hr forecast. The four free parameters are not changed from their previous Cabauw-case values. The radiation divergence is applied during the 'dynamics' parts of each forecast step to cause heating or cooling in various parts of the domain, and then is followed by the usual transilient turbulent mixing.

5.1.1. *Longwave Forcings Only (Nocturnal Stratocumulus Case)*

Figure 13b shows that the effect of cloud-top cooling dominates over cloud-base heating, causing convective mixing between cloud top and the ground. In this mixed layer, θ decreases with height by about 0.5 °C per km on the average, with a greater

superadiabatic lapse rate near cloud top. The grid point at cloud base is heated by radiation to about 0.2 °C above the surrounding potential temperatures. The dominant convection is obviously generated by upside-down thermals originating from the cold cloud top and descending all the way to the surface.

The turbulent heat flux profile (Figure 13a) exhibits the linear change of heat flux with height, as is expected for a well mixed layer. The discontinuities of turbulent heat flux at cloud base and cloud top are associated with the radiation flux jumps at those locations. It is clear from Figure 13c that the wind quickly adjusts to a nearly well mixed state, except for the frictionally-induced shear region in the surface layer.

5.1.2. *Combined Long and Short Wave Forcings (Daytime Stratocumulus)*

For this case, the longwave cooling at cloud top is less than the combined solar heating and longwave cloud base heating. The resulting net heating is shown in Figure 14a. As a result of the cooling at cloud top and the heating just below cloud top, a strong superadiabatic lapse rate develops just below cloud top (Figure 14b). The warming at cloud base is also evident. The corresponding turbulent heat flux profile is shown in Figure 14a.

For this case, the thermals generated by cloud-top cooling mix both the cloud and subcloud layers into one mixed layer. However, Figure 14c shows that the mixing below cloud base is slightly less intense than the mixing within the cloud, resulting in slightly enhanced shear below cloud base.

5.2. Neutral boundary layer

For this idealized case, a geostrophic wind of $U_g = 5\ \mathrm{m\ s^{-1}}$. $V_g = 0$ is applied at all heights. The initial winds are set equal to the geostrophic values. The initial temperature is adiabatic, with no heating or cooling applied during the forecast. There is no horizontal advection of heat or momentum. The only boundary condition applied is friction at the ground, using the drag relationship used for the Cabauw case studies. A grid spacing of 20 m is used within a vertical domain of 1000 m, and a 10 m timestep.

The precise shape of the resulting wind profile was found to depend on the value of the timescale, T_0. For $T_0 = 1000$ s as in the Cabauw simulations, the wind speed smoothly increased from zero at the surface to the geostrophic value at the top of the domain. For a smaller value of $T_0 = 100$ s, the wind approached geostrophic at a much lower altitude, at about 300 m (Figure 15a). Thus, in the absence of temperature inversions and thermal forcings to define or limit turbulent domains, it appears that T_0 effectively defines the domain. Although T_0 = constant was used in the study here, one might wish to parameterize T_0 as a function of relevant scales, such as z/u_* in the surface layer.

The simulation quickly approaches a quasi-steady state giving an approximately logarithmic change of wind speed with height (Figure 15a). When plotted on a semi-log graph (Figure 15c), it is obvious that the lowest two points fall on the straight line associated with the roughness length and stress for this case, but at higher altitudes the wind deviates from the surface-layer type profile to approach the geostrophic wind speed

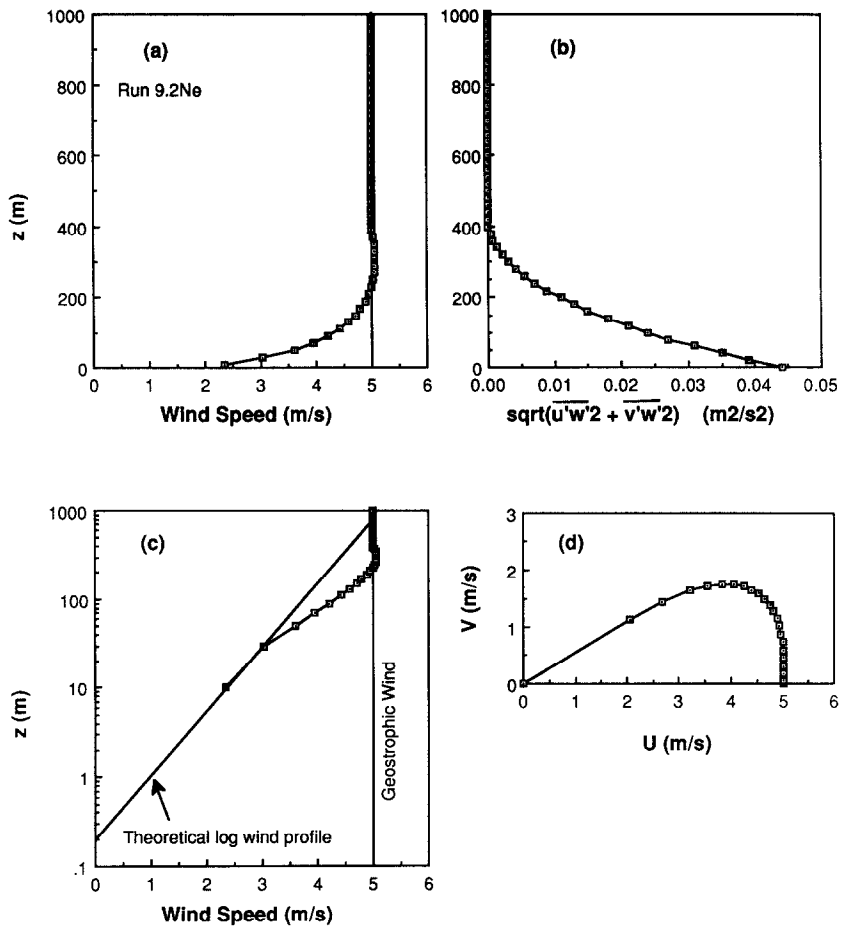

Fig. 15. Simulation of a neutral boundary layer (run 9.2Ne). All plots show the state at 6 hr into the simulation (an approximate steady state was reached after the first hour). Wind speed profiles are shown on (a) linear and (c) semilog graphs. The magnitude of the vertical flux of horizontal momentum is shown in (b). A hodogram is shown in (d). In (c) are also shown the imposed geostrophic wind, and the theoretical (similarity) neutral log-wind profile for a roughness length of 0.2 m and stress equal to the surface value (where $u_* = 0.209$ m s^{-1}).

asymptotically. The momentum flux shows a smooth decrease from the surface value (u_*^2) to zero aloft (Figure 15b). When the U and V components are plotted as a hodogram (Figure 15d), they show a spiral shape with cross-isobaric flow at low altitudes.

6. Sensitivity Study

An extensive sensitivity study was performed, of which only the highlights are presented here. The Cabauw 30 May, 1978 case was used.

6.1. PARAMETERS

Of the original $(n^2 - n)$ degrees of freedom associated with independent coefficients in the transilient matrix, the parameterization outlined in Section 2 reduced the degrees of freedom to four: the parameters R_c, D, T_0, and Y_{ref}. The following values of these parameters were tested:

$$R_c = 0.21, 0.25, 1.0\,; \qquad D = 1, 10, 1000;$$

$$T_0 = 10, 100, 1000\text{ s}\,; \qquad Y_{ref} = 500, 1000, 2000\,.$$

The best combination of parameters is $R_c = 0.21$, $D = 1$, $T_0 = 100$ s, and $Y_{ref} = 1000$. The model is most sensitive to R_c, and least sensitive to Y_{ref}. Details are described below.

6.1.1. R_c

As the critical Richardson number, R_c, is increased, the domain of turbulence usually increases, the rate of growth of the mixed layer or turbulent stable boundary layer increases, and the intensity of mixing is greater. In particular, the stable boundary-layer forecast is more sensitive to R_c than is the mixed layer. For example, when $R_c = 1$, a 1300 m thick well-mixed layer formed at night, instead of the observed shallower stable layer on the order of 200 m thick. During the day, $R_c = 1$ caused the mixed-layer top to be about 8% (i.e., 200 m) higher than with $R_c = 0.21$.

Some modelers in the past have used larger values for the critical Richardson number with coarser grid spacings. It appears that this is unnecessary for the present transilient turbulence formulation because the transilient coefficient parameterization already includes a factor $\Delta t/(\Delta z)^2$. This automatically adjusts the turbulence to the grid spacing, making the resulting forecast quasi-independent of the resolution. As will be discussed at the end of this section, however, there is still some dependence on grid spacing that is intrinsic with the transilient approach.

6.1.2. T_0

Both the mixed layer and nocturnal boundary layer are moderately sensitive to T_0. For example, with $T_0 = 10$ s, the daytime 2 km thick convective mixed layer does not form, but instead turbulence is confined to a shallow 400 m layer near the ground. Within this layer are an unrealistically large (superadiabatic) lapse rate and surface temperature. The nocturnal boundary layer is not much better: there is no turbulence at all, and the cooling is impressed on the bottom grid point. When $T_0 = 100$ s, the forecast is already substantially better, yielding a mixed layer on the order of 2 km thick during the day, and a nocturnal boundary layer on the order of 200 m. There is only a slight further improvement when T_0 is increased to 1000 s. Although $T_0 = 1000$ s works best for the Cabauw case, we saw earlier that $T_0 = 100$ s works better for the neutral case.

6.1.3. D

Both stable and unstable boundary layers are moderately sensitive to D. If D is larger than 100, then dissipation is so great that static instabilities are unable to generate

sufficient turbulence, thereby leaving unrealistic superadiabatic lapse rates within the modeled domain. The stable boundary layer is very shallow, with no turbulence. For $D = 10$, both the convective and stable boundary layers are much more realistic, with only slight additional improvement for $D = 1$.

6.1.4. Y_{ref}

Larger Y_{ref} values enhance subgrid mixing at the expense of mixing across grid box boundaries. There was little noticeable change in the depth of the turbulence layer for the three values tested. Mean soundings also showed only minor differences, except near boundaries having strong forcings. Larger Y_{ref} values had slightly larger superadiabatic lapse rates at the surface for Cabauw, larger superadiabatic lapse rates at cloud top for the dry stratocumulus simulation, and slower speeds for the lowest grid point in the neutral simulation. The simulations were least sensitive to Y_{ref}.

6.1.5. *Sensitivity Discussion*

Of these four parameters, two are more or less bounded by physical constraints. The critical Richardson number is known to be somewhere within the range of 0.2 to 0.25, which is a strong reason for choosing $R_c = 0.21$. When examining the bulk properties of turbulence, it is also recognized that dissipation will roughly balance production. More production causes greater turbulence and therefore greater dissipation. For this reason, one would expect the dissipation factor, D, to be on the order of one.

The remaining parameters, T_0 and Y_{ref}, are more difficult to pin down. Arguments could be made in favor of scaling T_0 to convective time-scales during the day, to stable time-scales at night, to time-scales related to different size domains, and so forth. In fact, one could conceivably parameterize T_0 as a function of other variables. The main point to be made, however, is that even with a fixed value somewhere in the range of $100 \text{ s} \leq T_0 \leq 1000 \text{ s}$, the turbulence generated by the transilient parameterization is determined by the mean flow, and yields forecasts that are very reasonable for a variety of situations. By not imposing any preconceived scalings on T_0, we find that the transilient parameterization is not limited to the corresponding preconceived situations. This opens the possibility for the transilient approach to be used in operational models where the real boundary layer often does not fall into any idealized simple class.

6.2. Discretization

Sensitivity studies have been run with

$$\Delta z = 10, 50, 100, 200, \text{ and } 500 \text{ m},$$

$$\Delta t = 5, 10, 15, \text{ and } 30 \text{ min}.$$

The best forecasts occur for small Δz and small Δt, with $\Delta z/\Delta t > 0.1 \text{ m s}^{-1}$. Larger discretizations also yield very good forecasts, with great savings in computer costs. We feel that $\Delta t = 10$ min and $\Delta z = 50$ or 100 m yield a good compromise between resolution and computational speed for most boundary-layer forecasts. Details follow.

As was described by S3, the transilient turbulence scheme is absolutely numerically stable for any Δt and Δz. This was indeed verified by every simulation (over 100) that was run during the past three years. The discretization question is thus really one of accuracy vs computational time. Computer storage requirements and computational time for transilient parameterizations are discussed in more detail by Stull (1987).

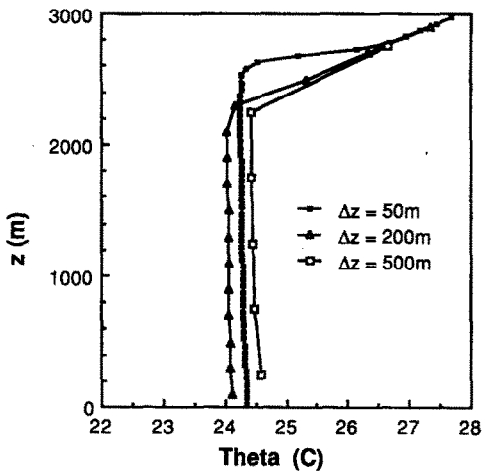

Fig. 16. Comparison of modeled potential temperature profiles 10 hours into the forecast of Cabauw case 1 (valid 1600 GMT on 30 May, 1978) for a variety of grid spacings.

Figure 16 shows the 30 May, 1978 Cabauw simulations valid at 1600 GMT for three different grid spacings. The forecasts give mixed layers of nearly the same depth (50 m difference) and temperature (0.5 °C difference) for resolutions of Δz = 200 m and Δz = 500. The forecast made with resolution Δz = 50 m showed a different height than the others because of the *destabilization problem* (see Section 6.3). The low-resolution simulation ran 100 times faster than the high-resolution one, but gave an evolving mixed layer nonetheless. Thus, the transilient parameterization could be used in a large-scale numerical weather forecast model where coarse grid spacings and long timesteps are imposed. For detailed studies of boundary-layer evolution, finer resolutions might be chosen.

6.3. Destabilization problem

The most significant problem of the transilient scheme is intrinsically related to the concept of splitting each timestep into a dynamics (dynamically destabilizing) portion, and a turbulence (dynamically stabilizing) portion. This is best illustrated by an example. Picture a convective mixed layer covering 10 grid points, where each grid point starts with the same potential temperature. Above those 10 grid points are other points within the capping stable layer. During any one timestep, the prescribed heat flux into the bottom point causes that point to warm during the dynamics portion of the step. Since

that point is now warmer than the 9 other mixed-layer points above it, the transilient portion of the timestep detects the resulting instability and mixes the warmer surface layer air up to the higher grid points in the mixed layer. Few if any of the grid points within the capping stable layer are affected.

If we start with the same initial condition, but with 100 grid points within the same depth of mixed layer, then the dynamics portion of the forecast will cause the bottom grid point to warm ten times as much as it did in the previous low resolution case. The reason is that the same prescribed flux is applied to a layer one tenth as thick. This bottom grid point is now not only warmer than all the other mixed-layer points above it, but it could also be warmer than a number of the grid points within the capping inversion. As a result, the transilient scheme will detect dynamic instabilities from the surface up to a level well within the capping inversion, resulting in entrainment of this warm capping air downward. The net result is greater entrainment, a larger negative heat flux near the top of the mixed layer, and a deeper warmer mixed layer than the previous case. Such a problem is evident in Figure 16, for $\Delta z = 50$ m.

The conclusion is that simulated entrainment rates are faster when Δz is smaller. Of course, if we were to take a smaller timestep, the lowest grid point would be warmed by a smaller amount and entrainment would be appropriately reduced. Thus, the entrainment rate is directly controlled by the ratio $\Delta z/\Delta t$. Based on our experience with various values of this ratio, we suggest that the discretization be chosen such that $\Delta z/\Delta t > 0.1 \text{ m s}^{-1}$.

Before leaving this topic, however, we should mention that real mixed layers exhibit via their superadiabatic surface layers a destabilization, which must first occur before convective turbulence can develop in response. This continuous process of destabilization and stabilization in the real atmosphere is not described precisely by a discrete approximation. Nevertheless, by choosing an appropriate ratio for $\Delta z/\Delta t$, we can artifically approximate this continuous process.

7. Discussion and Conclusions

An improved parameterization for the transilient coefficients has been presented that uses a simplified form of the turbulence kinetic energy (TKE) equation instead of using Richardson numbers. The second moment terms of the TKE equation are approximated by first moment (mean) variables, leaving the new parameterization as a non-local first-order closure. This approach is still classified as a *responsive* parameterization to the discrete form of transilient turbulence theory.

The relationship between the previous (S1) and the present approach can be approximated by first defining S, B, and Di to be the shear production, buoyancy, and dissipation terms of the TKE equation, respectively. If a transilient coefficient is represented by c and the critical Richardson number by R_c, then:

$$c \propto (1/S)[S - B/R_c] \qquad \text{(previous)},$$

$$c \propto [S - B/R_c] - Di \qquad \text{(present)}.$$

In the previous approach, small shears created large values of c because of the $(1/S)$ factor, regardless of the magnitude of $[S - B/R_c]$. This led to unrealistically large turbulence and mixing in some regions. The new approach, which still includes $[S - B/R_c]$, does not blow up as S approaches zero.

Also, the derivation for the new approach automatically gave a $\Delta t/[(i - j)\Delta z]^2$ factor times the $[S - B/R_c]$ term, which is required to yield solutions that are not dependent on Δt or Δz (see S3). In the previous approach, this factor was artifically included in the form of a weighting factor, w_{ij}.

In the previous approach, a distinction was made between onset and termination critical Richardson numbers. This was really a throwback to the turbulent adjustment concept that inspired the transilient theory. Setting onset and termination critical Richardson numbers to the same value slightly affects the sporadic nature of turbulence simulated, but has little effect on the forecast profiles of the mean variables. The present approach makes adequate forecasts with just one critical Richardson number.

The resulting improved transilient parameterization was tested in a simple 1-D grid-point model of the lower troposphere. This was applied to three case studies using data from the Cabauw tower in the Netherlands: one served to calibrate the four free parameters, the other two were independent tests. Idealized simulations were also performed for a neutral boundary layer, and two 'dry' stratocumulus idealizations.

There were no explicit equations for depth of the mixed layer, nor equations specifying that mixed layers should form and grow in conditions of surface heating, yet the simulations exhibited growing mixed layers with entrainment, not just encroachment. Mean profiles of potential temperature were very well mixed in the interior of the mixed layer, with non-zero lapse rates in the surface layer and the entrainment zone. Profiles of specific humidity and wind exhibited a slight slope within the interior of the mixed layers, in agreement with the signs of their respective fluxes at the top and bottom of the mixed layer. Near sunset, modeled turbulence decays over the bulk of the previous mixed layer, leaving a non-turbulent or slightly turbulent residual layer.

Development and evolution of stable boundary layers are very sensitive in the model to the initial conditions, the mechanical and thermal forcings, and to the time history of those forcings. On nights with strong winds, boundary-layer profiles evolve that appear relatively well mixed, while on nearly calm nights a very shallow stable boundary layer will form.

As a simple test of the importance of thermal forcings on the forecast, an idealized neutral boundary layer was modeled where there was no surface forcing other than drag. The resulting profile exhibited a slowing of the wind near the ground with a profile that was approximately, although not exactly, logarithmic. For heating and cooling imposed at the interior of the grid model, such as might be expected if there was radiative heating or cooling associated with clouds, the model developed mixed layers where cloud-top cooling was strong.

The parameterization described in this paper reduces the degrees of freedom from the $(n^2 - n)$ independent transilient coefficients to four (the parameters R_c, D, T_0, and Y_{ref}). Sensitivity studies were made for one of the Cabauw tower cases. It was found that the

stable boundary layer is most sensitive to R_c, while the mixed layer is most sensitive to T_0. Both were moderately sensitive to D, and relatively insensitive to Y_{ref}. The recommended values of the four parameters are: $R_c = 0.21$, $D = 1$, and $T_0 = 100$ s, and $Y_{ref} = 1000$.

Although the model is absolutely numerically stable, better forecasts are achieved when $\Delta z/\Delta t > 0.1$ m s^{-1}. Also, inaccurate simulations can occur when the timestep is long compared to the nonstationarity of the flow. For mixed layers, for example, it is recommended that $\Delta t \leq t_*$, where t_* is a convective time-scale on the order of 15 min.

Finally, the computation time is approximately proportional to n^2, where n is the number of grid points in the model. Since the computations involve matrix multiplications that are always performed regardless of the turbulent state of the atmosphere, the computations can be made very efficiently on a computer where the code can be vectorized. Even without such vectorization, computations are fast enough to be conveniently performed on microcomputers.

Additional research is presently being conducted in incorporating transilient turbulence into a 2-D cloud model, and into a 3-D mesoscale model. These latter tests utilize an unequally spaced vertical grid arrangement, and incorporate some of the deep convection processes into the transilient scheme. In addition to atmospheric applications, transilient turbulence theory is being concurrently tested in ocean models (Stull and Kraus, 1987; Gaspar *et al.*, 1987). Spectral and eigenvector implications are also being explored.

Acknowledgements

Discussions with Aad van Ulden, Frans Nieuwstadt, Han van Dop, Steve Nicholls, Hans Reiff, Peter Duynkerke, Bert Holtslag, and Philippe Gaspar were particularly helpful. The first author is especially grateful to the scientists at KNMI for the invitation to work with them on this project. Partial support was also provided by the USA National Science Foundation via grant ATM-8508759.

References

André, J.-C., DeMoor, G., Lacarrère, P., Therry, G., and du Vachet, R.: 1978, 'Modeling the 24-hour Evolution of the Mean and Turbulent Structures of the Planetary Boundary Layer', *J. Atmos. Sci.* **35**, 1861–1883.

Bhumralkar, C. M.: 1975, *A Survey of Parameterization Techniques for the Planetary Boundary Layer in Atmospheric Circulation Models*, ARPA Report R-1653-ARPA (order # 189–1), 84 pp.

Driedonks, A. G. M.: 1981: 'Dynamics of the Well-Mixed Atmospheric Boundary Layer', Doctoral Dissertation, Free University of Amsterdam, KNMI Scientific Report 81–2, KNMI, De Bilt, The Netherlands, 189 pp.

Driedonks, A. G. M.: 1982, 'Models and Observations of the Growth of the Atmospheric Boundary Layer', *Boundary-Layer Meteorol.* **23**, 283–306.

Driedonks, A. G. M. and Tennekes, H.: 1984, 'Entrainment Effects in the Well-Mixed Atmospheric Boundary Layer', *Boundary-Layer Meteorol.* **30**, 75–105.

Driedonks, A. G. M., van Dop, H., and Kohsiek, W.: 1978, 'Meteorological Observation on the 213 m Mast at Cabauw in the Netherlands', Preprints from the Fourth Symp. on Meteor. Obs. and Instr., Denver, U.S.A., Amer. Meteor. Soc., Boston, U.S.A., pp. 41–46.

Gaspar, Ph., Stull, R., and Boissier, Ch.: 1987, Long-Term Simulation of the Upper Ocean Mixing Using Transilient Turbulence Theory', *International Liège Colloquium on Ocean Hydrodynamics, Belgium*, 150 pp.

Loius, J. F.: 1979, 'A Parametric Model of Vertical Eddy Fluxes in the Atmospheric', *Boundary-Layer Meteorol.* **17**, 187–202.

Mellor, G. L. and Yamada, T.: 1982, 'Development of a Turbulence Closure Model for Geophysical Fluid Problems', *Rev. Geophys. Space Phys.* **20**, 851–875.

Nieuwstadt, F. T. M.: 1984, 'Some Aspects of the Turbulent Stable Boundary Layer', *Boundary-Layer Meteorol.* **30**, 31–56.

Nieuwstadt, F. T. M. and Brost, R. A.: 1986, 'The Decay of Convective Turbulence', *J. Atmos. Sci.* **43**, 532–546.

Stull, R. B.: 1976, 'Mixed-Layer Depth Model Based on Turbulent Energetics', *J. Atmos. Sci.* **33**, 1268–1278.

Stull, R. B.: 1984, 'Transilient Turbulence Theory. Part I: The Concept of Eddy Mixing Across Finite Distances', *J. Atmos. Sci.* **41**, 3351–3367.

Stull, R. B.: 1986, 'Transilient Turbulence Theory. Part III: Bulk Dispersion Rate and Numerical Stability', *J. Atmos. Sci.* **43**, 50–57.

Stull, R. B.: 1987, 'Transilient Turbulence Algorithms to Model Mixing Across Finite Distances', *Environ. Software.***2**, 4–12.

Stull, R. B. and Hasegawa, T.: 1984, 'Transilient Turbulence Theory. Part II: Turbulent Adjustment', *J. Atmos. Sci.* **41**, 3368–3379.

Stull, R. B. and Kraus, E.: 1987, 'The Transilient Model of the Upper Ocean', *J. Geophys. Res. Oceans* (in press).

Wyngaard, J. C.: 1982, 'Boundary Layer Modeling', in F. T. M. Nieuwstadt and H. van Dop (eds.), *Atmospheric Turbulence and Air Pollution Modelling*, D. Reidel Publ. Co., Dordrecht, Holland, pp. 69–1061.

Wyngaard, J. C. and Brost, R. A.: 1984, 'Top-Down and Bottom-Up Diffusion of a Scalar in the Convective Boundary Layer', *J. Atmos. Sci.* **41**, 102–112.

Zeman, O.: 1981, 'Progress in the Modeling of Planetary Boundary Layers', *Ann. Rev. Fluid Mech.* **13**, 253–272.